Article:

Sanvitale, N., Bowman, E. orcid.org/0000-0001-7868-6688 and Cabrera, M.A. (2021) Experimental investigation on the impact dynamics of saturated granular flows on rigid barriers. Environmental and Engineering Geoscience, 27 (1). pp. 127-138. ISSN 1078-7275

https://doi.org/10.2113/EEG-D-20-00033

Experimental investigation on the impact dynamics of saturated granular flows on rigid barriers

Nicoletta Sanvitale[a,*], Elisabeth Bowman[a], Miguel Angel Cabrera[b]

[a]*University of Sheffield, Sir Frederick Mappin Building, Mappin St., Sheffield, S1 3JD, UK*

[b]*Universidad de los Andes, Carrera 1 Este No. 19ª-40, Bogotá, 111711, Colombia*

Abstract

Debris flows involve the high speed downslope motion of rocks, soil and water. Their high flow velocity, and high potential for impact loading make them one of the most hazardous of gravitational mass flows. This paper focuses on the role of particle size grading and degree of fluid saturation on impact behaviour of fluid saturated granular flows on a model rigid barrier in a small scale flume. The use of a transparent debris-flow model and Plane Laser Induced Fluorescence allows the motion of particles and fluid within the medium to be examined and tracked using image processing. In this paper, experiments are conducted of flows consisting of two uniform and one well graded particle size gradings at three different fluid contents. The evolution of the velocity profiles, impact load, bed normal pressure and fluid pore pressure for the different flows are measured and analysed in order to gain a quantitative comparison of their behaviour before, during and after impact.

1. Introduction

A debris flow is a rapid surging mass of non-plastic soil, rock and water in a steep channel that may present high impact load and long runout (Iverson, 1997; Takahashi, 2007; Hungr et al., 2013). A common approach to prevent these flows from reaching vulnerable areas is by obstructing their channelized paths with engineered barriers, which trap most of the transported debris, dampening the overall flow inertia, and, therefore, decreasing their expected runout. These barriers can be rigid walls or flexible nets, with their main goal being to withstand the impact forces from the transported debris and suspended (fluidized) material. Rigid barriers, also called check dams or sometimes catching dams, are the most common mitigation structure against debris flows, due to the minimal technical skills required in their construction and relative ease of obtaining building materials for reinforced concrete (Hübl et al., 2009).

The mechanics of debris flows depends on the interactions between the solid and fluid phase, which involves frictional, collisional and viscous stress transfer between particles and fluid, as well as flow-bed interactions for both particles and fluid. While the estimation of the pressures generated by the impact of debris flows on civil engineering structures has been widely investigated (Moriguci et al., 2009, Armanini et al., 2011; Bugnion et al., 2011; Hu et al., 2011; Scheidl et al, 2012; Cui et al., 2015; Zhou et al., 2018), the state of knowledge is still insufficient to accurately understand the effect of solid-fluid interactions on the dynamics and load evolution of the impact process. As a result, design approaches tend to be semi-empirical (Armanini 1997; Van Dine, 1996; Zhang, 1993; Arattano and Franzi, 1993).

The current paper presents the results of experiments using transparent analogue debris flows in a small-scale flume, aimed at investigating the bulk impact forces on rigid barriers. Granular flows with different particle size distributions and fluid content are adopted for the tests. The dynamics of the impact against a rigid barrier normal to the flow direction is observed via Planar Laser Induced Fluorescence, PLIF (Sthor et al., 2003; Sanvitale & Bowman, 2012). Impact forces against the obstacle, the basal total and fluid pressures, flow height and the mid cross-sectional flow dynamics at impact are recorded and discussed.

2. Experimental set up

Before testing, the fluid saturated granular material is stored in a rectangular sealed tank at the top of the channel. The material is gently agitated by hand within the tank to ensure consolidation is avoided, prior to manually releasing a sluice gate. The material flows down the 2.57 m long and 150 mm wide rectangular flume, whose angle of inclination can be adjusted, and which is set at 20º for the tests described here (see Figure 1). The barrier model is made of a 10 mm thick, 145 mm wide and 190 mm tall PMMA (acrylic) plate mounted perpendicularly to the base (see inset in Figure 1). This enables the barrier to effectively cross the full width of the flume but be unaffected by wall interactions. The plate is centrally connected via an aluminum support at the base to an axial load cell (U9C, HBM) and fixed to a linear bearing (LZMHS12-37T2P1, SKF). The barrier model is fixed to the flume bed at 2.25 m from the gate release. The sidewalls of the channel are made of borosilicate glass and the bottom of the flume is roughened with 3D-printed PLA (polylactic acid) plates with a hexagonal packing of 3 mm semi-spheres. The roughened bed is instrumented along its base with three pore pressure transducers, denoted PPT2, 3 and 4 (PDCR 810 Druck) and a load cell (LUX-B-ID Kyowa) with a top circular sensing plate of 23 mm diameter. PPT2 is located 350mm upslope from the end of the flume. Pore pressure sensor PPT2 and the load cell are located closest to the barrier at 75 mm distance from it and 30 mm either side of the centerline. The transducers PPT3 and PPT4 are located 175 mm and 350 mm further upslope from PPT2, respectively. All basal sensors have 3D printed disk headings, equivalent to the roughness of the rest of the base with the top of the heading flush with the base.

A 0.5 mm thick 532 nm laser light sheet is allowed to pass through a slit cut in the roughened bed and barrier model base, illuminating the flowing material along the flume centerline. The laser used is an Opus Quantum 532 producing continuous illumination at a power of approximately 1.5 W. The laser beam is positioned perpendicular to the bottom of the flume via a mirror then sent through three uncoated plano-convex cylindrical lenses (purchased from www.thorlabs.com) that spreads the beam into a light sheet. The length of the illuminated flume section is approximately 130-150mm. A high-speed camera (Miro M310) located close to the end of the flume records video of the illuminated cross-section at 2000 frames per second with a resolution of 1280 x 800 pixels. A long pass filter is placed over the lens to transmit only the fluorescence signal and discard the reflected laser light (Sanvitale and Bowman, 2012).

2.1. Materials

The PLIF technique relies on the use of a laser sheet to excite the fluorescence of a dye diluted in the fluid, and hence create an illuminated plane within the flow in which particles appear as dark shapes against a bright background. For the PLIF technique to work under optimum conditions, the refractive indices of the fluid and solid should match. The current experiments are performed with hydrocarbon oil (Cargille laboratories) dyed with a fluorescent powder, Nile Red, and mixed with borosilicate glass beads (Sigmund Lindner GmbH). The fluid has a kinematic viscosity that is 16 times higher than water (16 cSt at 25 °C) and a density that is 1.182 times lower (0.846 g/cm^3), such that mixture consolidation behavior is equivalent to that using quartz particles that one quarter the diameter in water. See Sanvitale & Bowman (2012) for further details on the experimental technique.

Three granular materials consisting of spherical borosilicate glass beads are used in these experiments: two uniform particle size distributions, PSD1 and PSD2, with glass beads of 3 mm and 7.5 mm respectively, and a more well graded sample, PSD3 (coefficient of uniformity $C_U = d_{60}/d_{10} = 5$, where d_x denotes the percentage passing by mass), with mean particle size of 7.5 mm (Figure 2). These samples are intended to provide an insight on the effects of particle size and gradation on the impact dynamics. The influence on the flow dynamics and impact of the fluid content are also investigated by setting the initial fluid content f_c, defined as $mass_{fluid}/mass_{solid}$ to 24%, 28% and 32%, for each solid material investigated (equivalent to solid volume fractions of 0.61, 0.58 and 0.54, respectively). Hence, we report the results of nine experiments in all.

2.2. Test procedure

Prior to each experiment, the flume is cleaned, avoiding the presence of dirt and oil films on the roughened bed and sidewalls. For each experiment exactly 10 kg of solid mass is used (Table 1). Oil to the desired fluid content is poured into the container and gently mixed with the glass beads to reduce the entrainment of air bubbles that would otherwise reduce optical transparency. Agitation of the mixture is maintained while the laser beam is set on, the high-speed camera is activated, and the sluice gate is opened. At release, a triggering shutter connected to the gate activates the sensors that record at a sampling rate of 36 kHz, for a duration of 9 s. Low pass filters are applied to the outcomes as described in Section 3.2.

3. Results and discussion

3.1. Impact kinematics

Figure 3 shows images of the flow impact for each PSD at different fluid content, f_c 24% for PSD1 and PSD2 and f_c 32% for PSD3 (images for the other tests are not shown for brevity). The flow direction is from right to left. The images show different instants during the impact of the mixture against the barrier with respect to the time t=0 at which the sluice gate was opened. For all the tests the impact process is characterized by a first stage during which individual saltating particles impact the wall before the arrival of the flow front. For the test using PSD3, due to the segregation of the different particle sizes during downslope shearing (Sanvitale and Bowman, 2012; 2017), larger particles accumulate at the front.

The images show the three different impact mechanisms (Armanini et al., 2011; Choi et al., 2015; Gray et al., 2003; Faug et al., 2015; Albaba et al, 2018) observed during experiments. The first mechanism (Fig 3(a)) is displayed only by PSD1 (uniform grain size of 3 mm beads) at f_c 24% and consists of a type of pile up process. The surge front impacts the rigid barrier and deposits at the base, then the subsequent flow material impacts and piles up on top of the existing deposits. When the maximum pileup height is reached the impact process rapidly attenuates. The second mechanism (Fig 3(b)) is characterized after the impact by the formation of a reflected wave propagating upstream. The third mechanism (Fig 3(c)) consists of the formation of a vertical jet travelling parallel to the vertical barrier that subsequently falls backward on the incoming surge, creating a secondary surge that propagates upstream.

For PSD2 and PSD3 at f_c 24% we observe the formation of a reflected wave, while at f_c 28% and 32%, we observed the jet like behavior. The test for PSD1 at f_c 28% shows an intermediate behavior with a formation of an initially small jet that, once it falls back on itself, creates a small surge propagating upstream that is immediately stopped by the incoming flow. Subsequently the impact of the incoming flow transitions more to be a type of reflected wave.

Figure 3 also shows the results of the corresponding Particle Image Velocimetry (PIV) analyses (Thielicke et al., 2014; Thielicke, 2014) conducted via image processing at specific stages on flow impact. The velocity field shown via the quiver plots (quiver lengths proportional to speed) displays the kinematics that are characteristic of the observed mechanisms.

The velocity $v_{i,}$ which is the average speed of the front of the incoming surge approaching the barrier before impact, is listed in Table 2. The front velocity is generally higher at larger fluid content. For the uniform gradings, at the same fluid content, the velocities are higher for a larger particle size, i.e. for PSD2 than PSD1. For the well-graded material, PSD3, with the same mean particle size as PSD2, the front velocity is much lower, but it is higher than for PSD1 tests. The bed roughness may play a role in the observed flow kinematics (Ahmadipur et al. 2019; Goujon et al., 2003; Silbert et al., 2001) with the scale of roughness of the 3 mm semi-spheres on the base inducing greater shearing within the uniform mixture of 3 mm beads in PSD1 compared to the 7.5 mm beads in PSD2. Tests with mixture PSD3 having 50% (by mass) particles larger than 7.5 mm and 50% smaller, produce lower flow velocities than for PSD2. In these tests, the presence of finer particles may have a dampening effect on large particle collisions, hence dissipate more energy within the body.

The Froude number, Fr:

$$Fr = \frac{v_i}{\sqrt{gcos \quad _i}} \tag{1}$$

where h_i is the flow depth of the incident surge, and θ the slope of the channel, quantifies the ratio between the inertial and gravitational forces. Table 2 reports the Froude numbers calculated for the experiments. The Fr results lie in the range between 0.90 and 4.86 – with values lying closer together for the larger particle sizes. In all cases, Fr increases with fluid content, due both to increased velocity and reduced flow height.

Armanini et al. (2011 and 2019) found that the nature of the impact depends on the Froude number of the incoming front; when gravity dominates over inertia there is a formation of a reflected wave, whereas when inertia dominates, jet-like behaviour up the wall occurs upon impact. Specifically, Armanini et al. (2019) analyzed the dynamic impact of water and mixtures of water and sediments of a specific PSD (d_{30} = 2.0 mm, d_{50} = 3.5 mm, d_{90} = 9.0 mm) on a barrier wall normal to flow. They found that for Fr $<\sim$ 3, a reflected wave forms, otherwise a vertical jet is produced. This finding is not in complete agreement with our results (Table 2), especially for the mixture PSD2, for which we observed a reflected wave impact at f_c of 24%, corresponding to Fr > 3. The transition from reflected wave to jet-behaviour lies in the Fr 3 to 4 zone but is influenced also by particle distribution and fluid content.

Figure 4 shows the evolution of the flow height at the barrier measured on the video footages (note the truncation of the plotted height for heights greater than the wall). PSD2 exhibits the greatest height at the barrier at the end of the test, which explains the greater final static load compared to the other mixtures. PSD2 at fc 28% and 32% are able to overtop the barrier.

Overtopping also occurs for PSD3 at fc 32% in the final part of the event due to the large fluid content, well above that needed to fully saturate (i.e. fill the voids between particles) the mixture, so that it can flow easily towards the barrier, increasing the height of the free surface of the fluid at values higher than the top of the wall.

The PSD3 at fc 28% test displays a initial height peak at 0.28 s, which is due to the vertical jet travelling up the wall at the beginning of the impact. After that a second spike follows at t = 1.1 s, due to the accumulation of fluid behind the barrier at the end of the impact, as occurred for the test PSD3 at fc 32%. This excess of fluid after reaching the barrier is reflected and move upslope.

The height of PSD1 tests is always lower than barrier and reaches values at the end of the tests comparable with PSD3.

3.2. Barrier load

The recorded raw barrier load signals present high frequency spikes that are due to random effects depending on the resonance frequency of the load cell and on the single instantaneous impact of large particles. In order to filter the data, we followed the procedure proposed by Scheidl et al. (2012), applying a low pass filter with a maximum high frequency. This high frequency is estimated considering the average maximum front velocity v_i, from the PIV analysis, and the maximum particle diameter, as $f_i=v_f$ / d_{max}. For PSD3 d_{max} has been take as d_{90} = 20mm. The resulting low pass filters for each test are listed in Table 1.

Time histories for measured basal pressures and barrier loads for all tests are given in Figures 5 (fluid content f_c 24%), Figure 6 (f_c 28%) and Figure 7 (f_c 32%). In each case, the load on the barrier is characterized by an initial dynamic phase and a subsequent final static value. The dynamic phase is due to the impact loading exerted by the incoming flow against the barrier while the static value is given by the pressure exerted by the deposited material behind the wall at the end of the event.

The tests with f_c 24% for all particle size distributions exhibit a gradual increase of the barrier load due to the continuous accumulation of the material behind the barrier. The PSD2 and PSD3 tests show many spikes in the signal related to the instantaneous impacts of single large beads. The highest peak force is reached by the PSD2 tests because for these mixtures, more material is able to reach the barrier, increasing the height of the static deposit (Figure 4). The high mobility of these flows is confirmed by their front velocities that are highest for all fluid contents (Table 1). Furthermore, it has to be noted that for the same mass of dry particles the fluid necessary to saturate the sample is different for the three PSDs. Before testing we measured that the saturation of the sample in the tank is reached with 22%, 20% and 13% of fluid content for the 3mm, 7.5mm and the well graded mixture, respectively. Hence the fluid content in excess of saturation that is available to fluidize the mixture is potentially higher for larger bead size (note that this picture becomes less clear for the well graded material, PSD3, due to segregation as the flow develops).

The tests at f_c 28% exhibit larger Froude numbers (2.3, 3.9, and 3.3 for PSD1, 2 and 3, respectively) and the observed impact mechanism consists of the formation of a vertical jet for PSD2 and PSD3. In these tests, during their dynamic interaction with the barrier, the flows develop a spike on the barrier load curve corresponding to the instant at which the jet falls back on the free surface of the incoming flow (Figure 6). This peak is followed by a transient decrease of the load due to the energy dissipation caused by the hydraulic jump subsequent to the falling jet breaking on the flow surface. For the PSD2 test, this spike represents the highest force, being larger than the final static load. For the PSD3 test before the impulse due to the falling jet, the barrier experiences a series of load peaks due to the largest particles accumulating at the front (due to particle size segregation) and colliding with the wall, although these transient peaks are lower than the final static load exerted on the wall by the total material accumulated during the event.

Intermediate to this, for the PSD1 at fc 28%, the flow impact produces an initial small jet that gives rise to the formation of a surge propagating upstream. This is then stopped by the incoming flow to evolve into a type of reflected wave.

The tests at f_c 32% for all the PSDs show that the impact mechanism is always jet-like at larger Froude numbers. At this fluid content the PSD1 mixture exhibits the largest front velocity and after a sudden increase of the barrier load when the flow front arrives, it develops a vertical jet with a corresponding increase of the barrier force up to a maximum when the falling jet breaks on the incoming flow. After this peak, the energy dissipation due to the formation of the hydraulic jump, leads to a decreasing load that is followed by a gradual growth due to the accumulation of the material from the tail of the debris flow surge. For PSD2 and PSD3 which have larger particles, the fluid content has les influence on the flow behaviour. PSD2 at f_c 32% shows the highest run up of the vertical jet, which results both in some material overtopping it and a higher barrier load when the falling jet breaks. The well graded material, PSD3, shows a similar impact behavior compared to that with f_c 28%, the main difference being a greater final static load due to more material being mobilized to reach the barrier.

The influence of the particle size on the response of the barrier is clear. PSD2, the uniform flows with the 7.5 mm particles, generate the greatest loads. For the well graded PSD3 tests, similar to PSD2, a number of spikes in the barrier signal are recorded from the load cell, representing collisions of large particles against the barrier; however, both the peak force during and after the impact reach final values similar to those of PSD1 mixture. The peak load due to the initial dynamic impact of the flows appears to be enhanced by the presence of a larger quantity of fluid for all the mixtures. In fact, the higher fluid content allows the mixtures to be more fluidised and hence to reach higher velocities when they move downslope. The larger fluid content also enhances the mobility of the flows, increasing the final static load at the end of the impact due to the greater accumulation of the material behind the wall (Figure 4).

Only the PSD2 (uniform, 7.5mm) tests exhibit a consistently higher peak barrier load from the initial dynamic impact than the static load exerted from the material deposited subsequently. The reason for this is that once they hit the barrier at high speed (Table 2), they produce a higher jet wave than other tests, with large particles that are easily mobilized and pushed upward against the barrier. In contrast, it is clear from the high speed images, that for the f_c 28% tests with PSD3, most of the top part of the runup wave is comprised of fluid as the large particles at the flow front are too heavy to be pushed any higher than approximately the middle height of the barrier (Figure 4). Furthermore, the presence of finer material can also have a damping effect on the large particle collisions. The combination of these factors can explain the similar value of the impact load between the 3 mm (PSD1) and the well graded (PSD3) tests.

3.3. Basal pressure development

Figures 5 to 7 show the responses of the pore pressure transducers using a running average filtering window of 400 data points and the evolution of the basal total pressure σ_{tot}. The PPT responses are dominated by the increase in the height of the fluid-saturated debris behind the barrier (which is effectively impermeable) after impact. Therefore, although flows initially pass over PPT4, then PPT3 and then PPT2 in succession on their descent motion (resulting in relatively small recorded pressures of the order of 0.2 kPa), PPT2 (closest to the barrier) then produces the largest and earliest response to this impact with recorded pressures ranging between 1 and 2 kPa except for the 3 mm test with f_c 24% characterized by pore pressure below 0.5 kPa. For all the tests at f_c 24% the impact is characterized by the arrival of an initially unsaturated flow front, for which the fluid pressure is absent due to the particles at the front running ahead of the fluid. This becomes more acute as the particle sizes segregate - with the largest particles trending to the front – as seen in field scale debris flows (Iverson, 1997).

Considering the measurements closest to the barrier (PPT2 and the basal load cell), differences are found in the pore pressure behaviour after the impact between flows at different fluid content, particularly for the 3mm flows (PSD1) which, considering the ratio of pore pressure to total stress, for f_c 24% shows the pore pressure to be always below hydrostatic, while for f_c 28% it is close to hydrostatic and for f_c 32% above hydrostatic immediately after the breaking of the falling jet.

For the well graded flows (PSD3) at both fluid content f_c 28% and 32% the pore pressures are much greater than hydrostatic until the hydraulic jump, developed after the breaking of the falling jet, ends. For the well graded flows at f_c 24%, after the arrival of the unsaturated front, the pore pressure is much larger than hydrostatic until the accumulation of the material behind the barrier occurs, then it drops to typical hydrostatic values. For the 7.5mm flows, the pore pressure is hydrostatic for f_c 24%, slightly above for 28% and largest for f_c 32%.

These results demonstrate that excess (i.e. greater than hydrostatic) pore pressures are not necessarily generated within uniform flows of spheres, except where sufficient fluid is present and sufficient agitation is generated (e.g. during an impact event). For well-graded flows (at least for the chosen grading and fluid contents examined here) excess pore pressures are both generated and maintained at impact. This is likely to be due to both larger particles agitating the flow upon impact and fines reducing the mixture permeability, hence maintaining the developed excess pore pressure for longer.

Conclusions

The paper presents an experimental investigation on the effects of fluid content and particle size on the impact force generated by a transparent debris-flow model on rigid barrier. The debris flow models were provided by using refractive index-matched mixtures of borosilicate glass beads in a Newtonian fluid. Small-scale flume experiments were carried out using a channel equipped on the bottom with three pore pressure transducers and a load cell for the measure of the total normal stress and fluid pore pressure. A rigid barrier, instrumented with another load cell, was fixed normal to the flume bed at 2.25 m from the gate release. The evolution of the impact load, bed normal pressure and fluid pore pressure for flows consisting of uniform and well graded particle size grading at three different fluid contents, 24%, 28% and 32%, was measured and analyzed. It has been found that excess pore pressures are not necessarily generated within uniform flows of spheres, except where sufficient fluid is present and sufficient agitation is generated (e.g. during an impact event). The particle size of the material has a strong influence on impact loading and overall response. The uniform flows with the largest particles generate the greatest load while for the well graded tests the presence of fine particles within the flow can provide a dampening influence. Larger fluid content leads to greater flow velocity and larger peak load in the initial dynamic phase of impact of the flows. Increasing the amount of the fluid content enhances also the overall mobility of the flows, increasing the final static load at the end of the impact due to the greater accumulation of the material behind the wall.

Acknowledgements

This research was supported through the Engineering and Physical Sciences Research Council (EPSRC), UK project no. EP/M017427/1 “High speed granular debris flows: new paradigms and interactions in geomechanics”. The authors would like to acknowledge the assistance of technicians at the University of Sheffield in the construction of the apparatus. MAC was partly funded by the Early-stage Researcher fund (FAPA) from the Universidad de Los Andes, under the Grant agreement No. PR.3.2016.3667.

References

Ahmadipur, A., Qiu, T., and Sheikh, B., 2019, Investigation of basal friction effects on impact force from a granular sliding mass to a rigid obstruction: *Landslides*, Vol. 16, pp.1089-1105, https://doi.org/10.1007/s10346-019-01156-0.

Albaba, A.; Lambert, S., and Faug, T., 2018, Dry granular avalanche impact force on a rigid wall: Analytic shock solution versus discrete element simulations: *Physical Review E*, Vol. 97 , No. 5.

Arattano, M., and Franzi, L., 2003, On the evaluation of debris flows dynamics by means of mathematical models: *Nat. Hazards Earth Syst. Sci.*, Vol. 3, No. 6, pp. 539–544, doi:10.5194/nhess-3-539-2003

Armanini, A., 1997, On the dynamic impact of debris flows. In Recent Development on Debris Flows, Armanini A, Michiue M (eds). Springer, Berlin, Vol. 64, pp 208–226.

Armanini A, Larcher M., and Odorizzi M., 2011, Dynamic Impact of a Debris Flow Front Against a Vertical Wall. In 5th International Conference on Debris-flow Hazard Mitigation, Genevois R, Douglas L (Editor). Casa Editrice Università La Sapienza: Roma, pp.1041–1049.

Armanini, A., Rossi, G., and Larcher M., 2019, Dynamic impact of a water and sediments surge against a rigid wall: *Journal of Hydraulic Research*, pp.1-12, doi: 10.1080/00221686.2019.1579113.

Bugnion, L., McArdell, B., Bartelt, P., and Wendeler, C., 2011, Measurements of hillslope debris-flow impact pressure on obstacles: *Landslides*, Vol. 9, No. 2, pp. 1–9, doi:10.1007/s10346-011-0294-4.

Choi, C. E., Au-Yeung, S. C. H., Ng, C.W.W., and Song, D. ,2015, Flume investigation of landslide granular debris and water runup mechanisms: *Géotechnique Letters,* Vol. 5, No. 1, pp. 28-32.

Cui, P., Zeng, C., and Lei, Y., 2015, Experimental analysis on the impact force of viscous debris flow: *Earth Surf. Processes Landforms*, Vol.40, pp. 1644–1655, doi:10.1002/esp.3744.

Faug, T.; Childs, P.; Wyburn E., and Einav, I., 2015, Standing jumps in shallow granular flows down smooth inclines: *Physics of Fluids*, Vol. 27, No. 7.

Gray, J.M.N.T.; Tai, Y.C., and Noelle, S., 2003, Shock waves, dead zones and particle-free regions in rapid granular free-surface flows: *Journal of Fluid Mechanics,* Vol. 491 , pp. 161-181

Goujon, C., Thomas, N. and Dalloz-Dubrujeaud, B., 2003, Monodisperse dry granular flows on inclined planes: role of roughness: *Eur Phys J E Soft Matter,* Vol. 11, No. 2, pp. 147-157. doi:10.1140/epje/i2003-10012-0. PMID: 15011055.

Hu, K., Wei, F., and Li,Y., 2011, Real-time measurement and preliminary analysis of debris-flow impact force at jiangjia ravine, china: *Earth Surf Process Landf.*, Vol. 36, pp. 1268–1278, doi:10.1002/esp.2155 .

Hubl, J., Suda, J., Proske, D., Kaitna, R., and Scheidl, C., 2009, Debris-flow impact estimation, In Proceedings of the 11th International Symposium on Water Management and Hydraulic Engineering, Ohrid, Macedonia.

Hungr, O., Leroueil, S., and Picarelli, L., 2013, The Varnes classification of landslide types, an update: *Landslides*, Vol. 11, pp. 167-194.

Iverson, R.M., 1997, The physics of debris flows: *Reviews of Geophysics*, Vol. 35, No. 3, pp. 245-296.

Iverson, R.M., George, D.L., and Logan, M., 2016, Debris-flow run-up on vertical barriers and adverse slopes: *Journal of Geophysical Research-Earth Surface*, Vol. 121, pp. 2333–2357, doi:10.1002/2016JF003933.

Moriguchi, S., Borja, R., Yashima, A., and Sawada, K., 2009, Estimating the impact force generated by granular flow on a rigid obstruction: *Acta Geotech*., Vol. 4, No. 1, pp. 57–71.

Sanvitale, N. and Bowman, E.T., 2012, Internal imaging of saturated granular free-surface flows: *International Journal of Physical Modelling in Geotechnics*, Vol. 12, No. 4, pp. 129-142.

Sanvitale, N. and Bowman, E.T., 2017, Visualization of dominant stress-transfer mechanisms in experimental debris flows of different particle-size distribution: *Canadian Geotechnical Journal*, Vol.54, No. 2, pp. 258-269.

Scheidl, C., Chiari, M., Kaitna, R., Mullegger, M., Krawtschuk, A., Zimmermann, T., and Proske, D., 2012, Analysing debris-flow impact models, based on a small scale modelling approach: *Surveys in Geophysics*, Vol. 34, No. 1, pp.121–40.

Silbert, L.E., Ertaş, D., Grest, G.S., Halsey, T.C., Levine, D. and Plimpton S.J., 2001, Granular flow down an inclined plane: Bagnold scaling and rheology: *Phys. Rev. E*, Vol. 64, No.5, doi:10.1103/PhysRevE.64.051302.

Stohr, M., Roth, K., and Jahne, B., 2003, Measurement of 3D porescale flow in index-matched porous media: *Experiments in Fluids*, Vol.35, No. 2, pp. 159–166.

Takahashi, T. 2007. *Debris flow: Mechanics, prediction and countermeasures*. Taylor & Francis.

Thielicke, W., and Stamhuis, E.J., 2014, PIVlab – Towards User-friendly, Affordable and Accurate Digital Particle Image Velocimetry in MATLAB: *Journal of Open Research Software,* 2(1):e30, doi: http://dx.doi.org/10.5334/jors.bl.

Thielicke, W., 2014, *The Flapping Flight of Birds - Analysis and Application*, Phd thesis, Rijksuniversiteit Groningen. http://irs.ub.rug.nl/ppn/382783069.

Van Dine, D.F., 1996, Debris flow control structures for forest engineering: Working paper, Ministry of Forest Research Program, Victoria, British Columbia

Zhang, S., 1993, A comprehensive approach to the observation and prevention of debris flows in china: *Natural Hazards*, Vol. 7, pp 1–23, doi:10.1007/BF00595676

Zhou, G.G.D., Song, D., Choi, C.E., Pasuto, A., Sun, Q.C., and Dai, D.F., 2018, Surge impact behaviour of granular flows: effects of water content: *Landslides*, Vol. 15, No. 4, pp. 695-709.

Figures

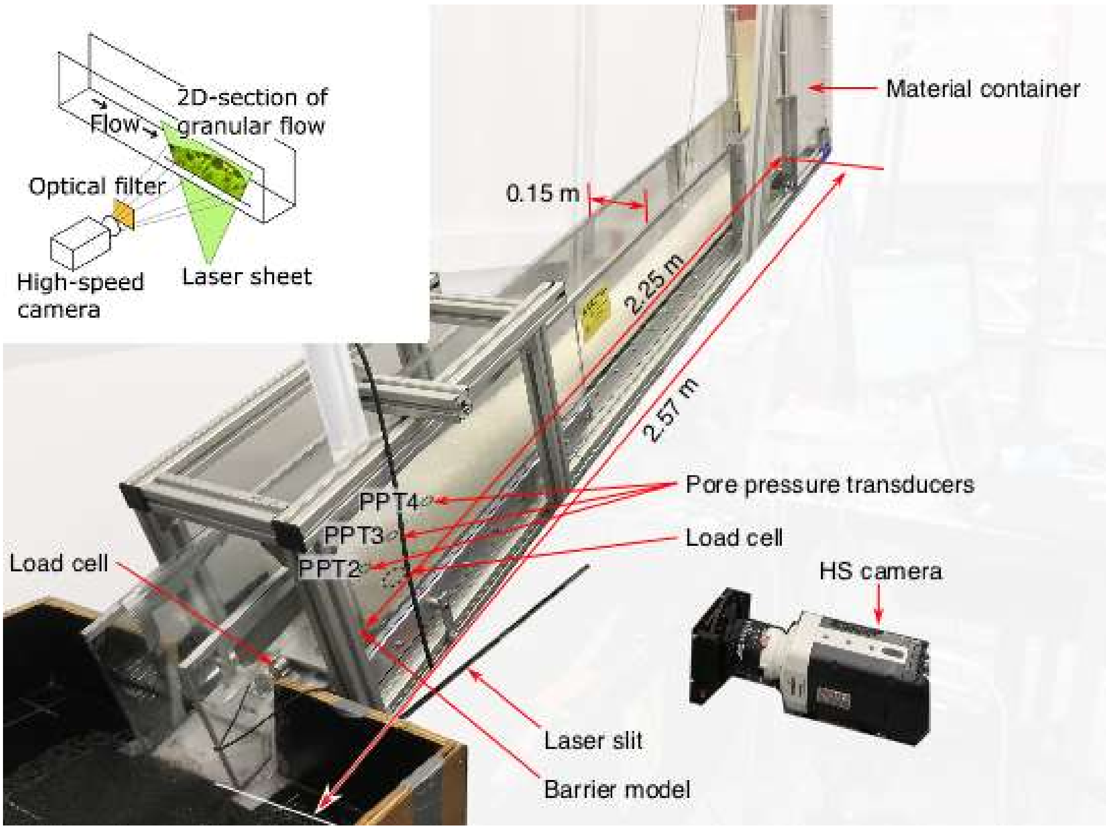

Figure 1. Apparatus employed in the tests. (Inset) PLIF setup

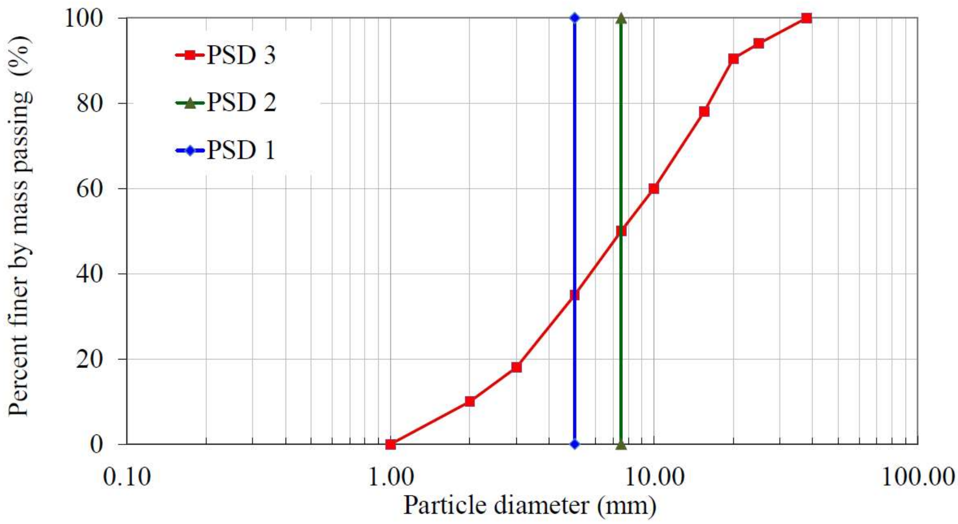

Figure 2. Particle size distributions (PSDs) for the solid materials used in the tests

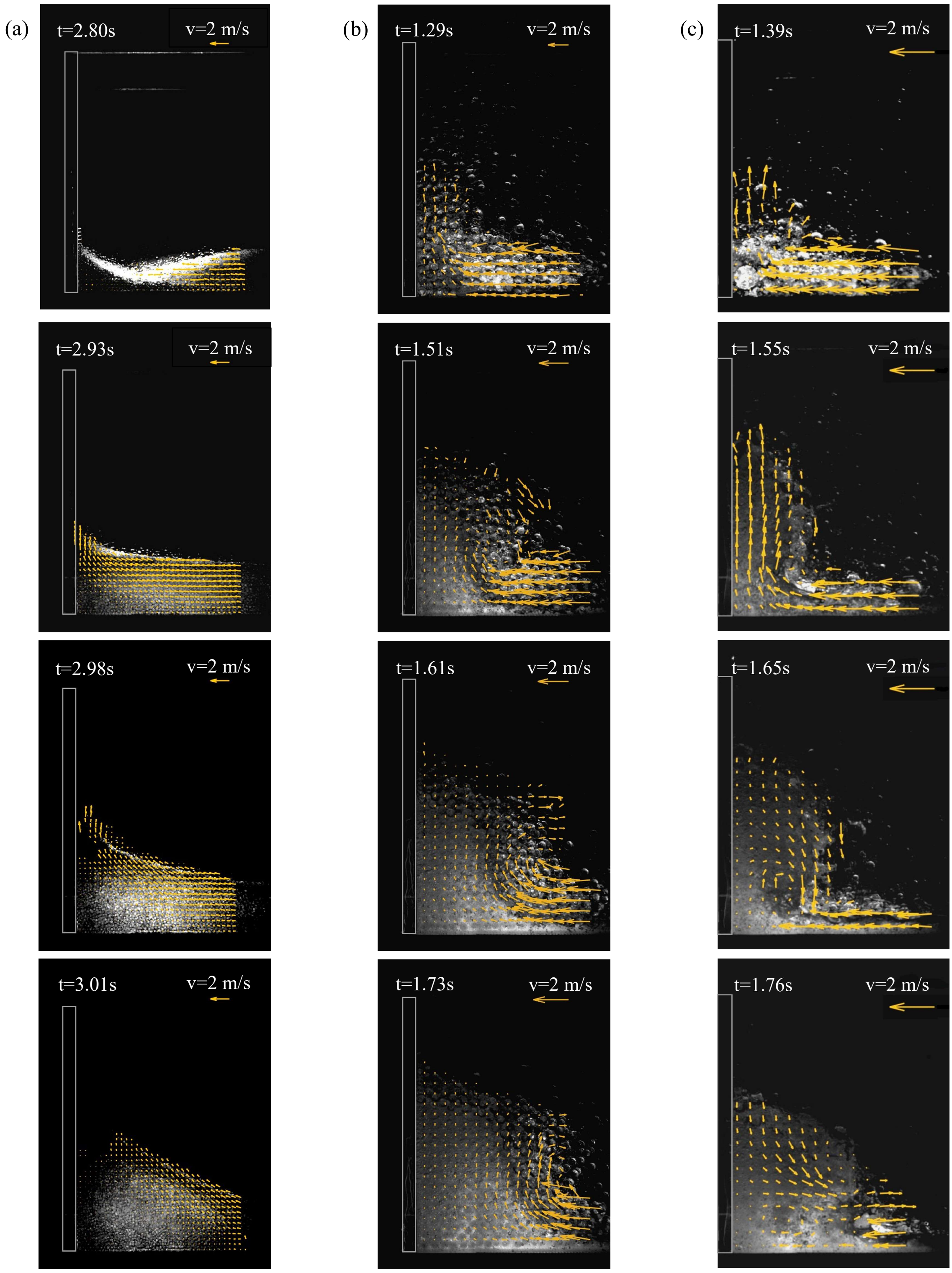

Figure 3. Sequences of the images recorded by the high speed camera for (a) PSD1 at fc of 24%, (b) PSD2 at fc of 24%, (c) PSD3 at fc of 32%. The overlapped arrows describe the corresponding velocity filed estimated using PIV analysis

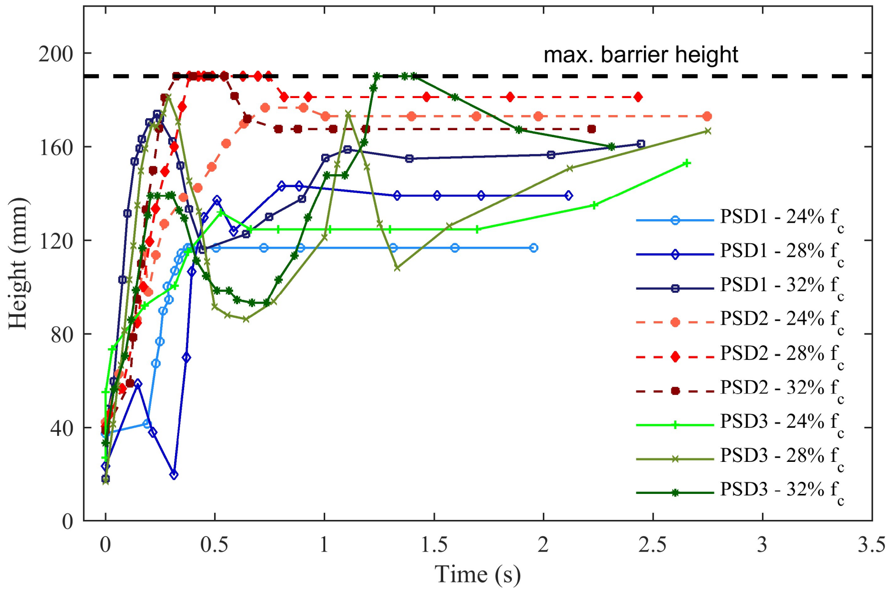

Figure 4. Measured run-up height at the barrier (time t=0 is the time of the flow front arrival)

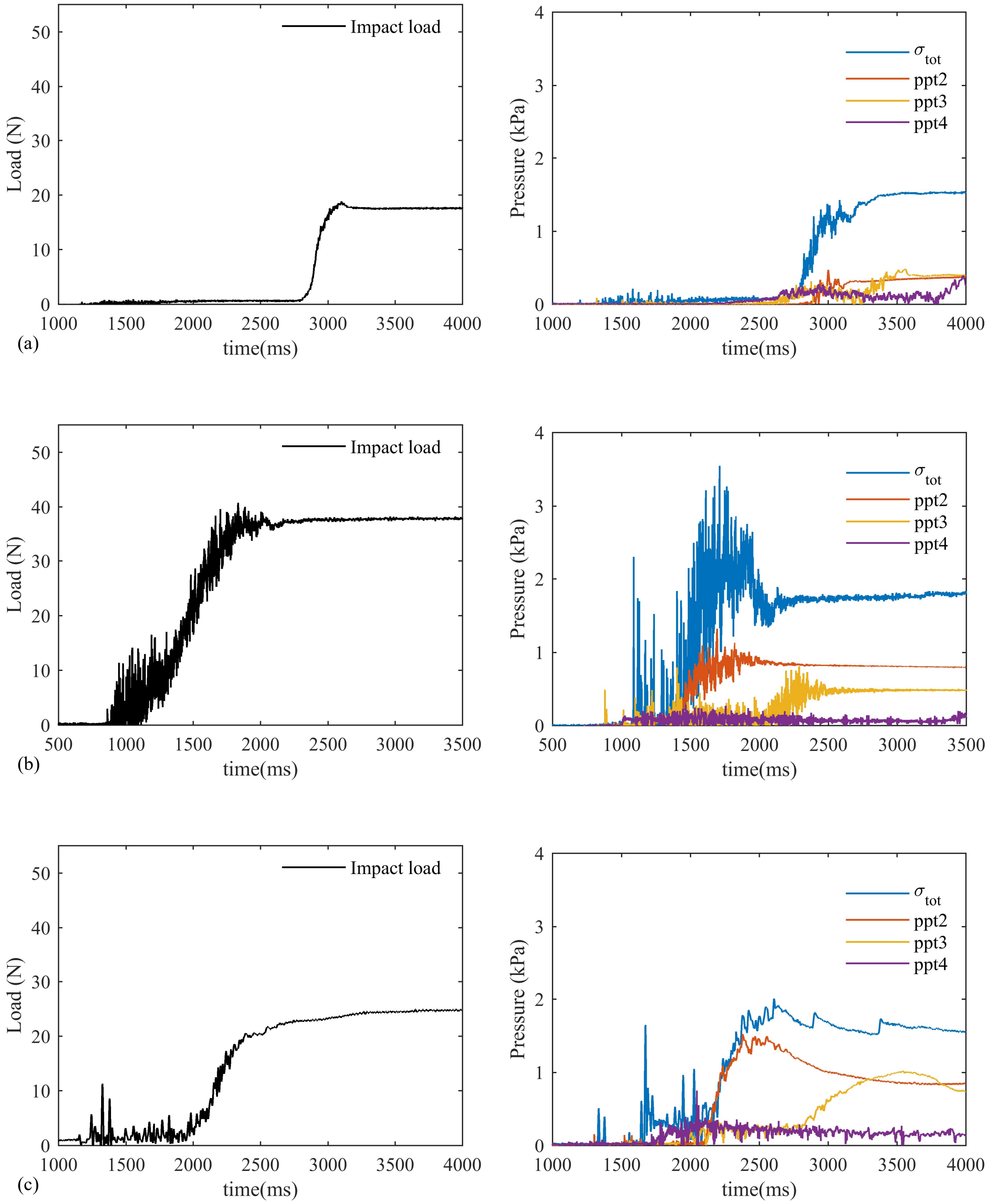

Figure 5. Fluid content 24% (Left) Load on barrier (Right) Basal pressures (a) PSD1, (b) PSD2, (c) PSD3

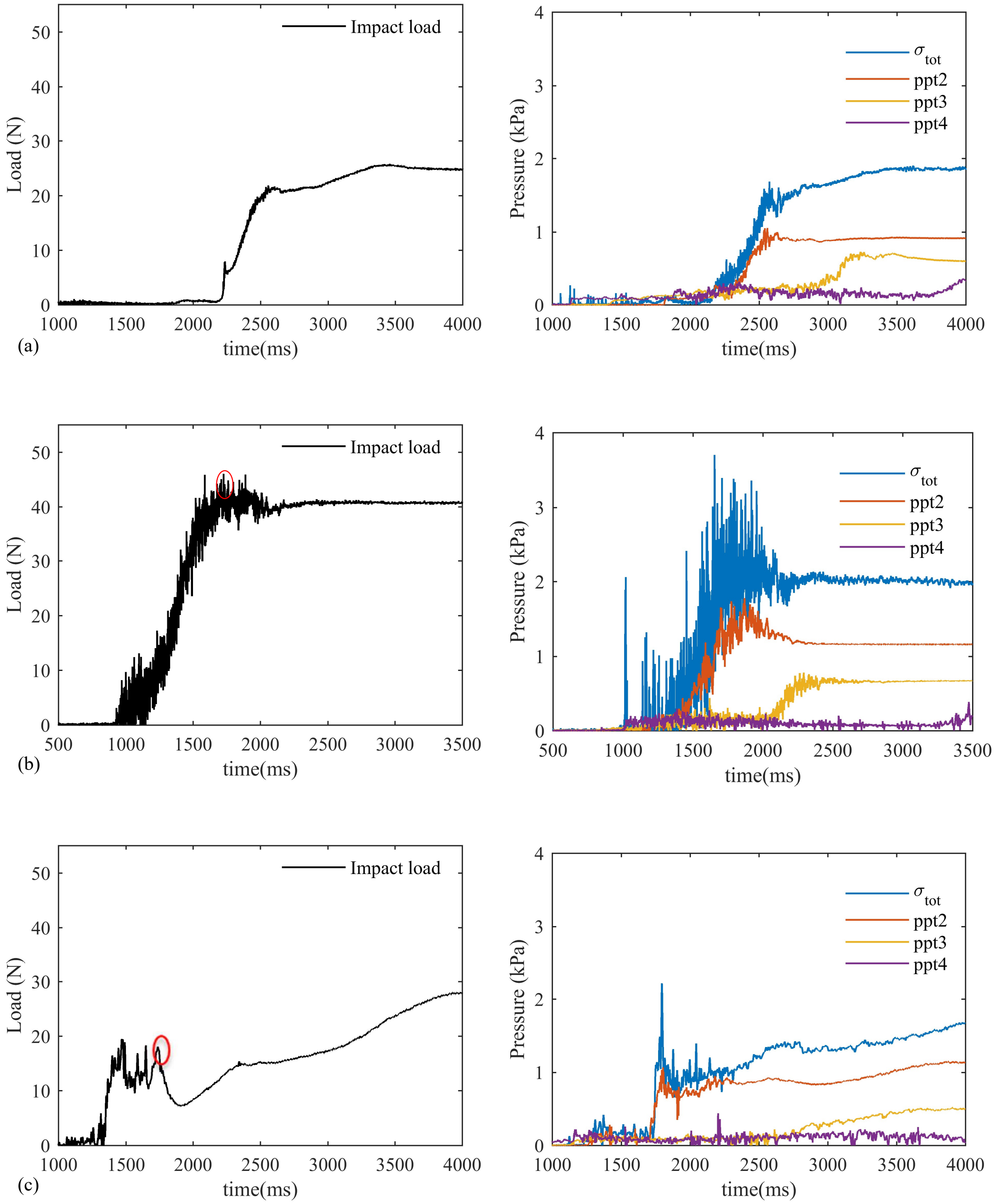

Figure 6. Fluid content 28% (Left) Load on barrier (Right) Basal pressures (a) PSD1, (b) PSD2, (c) PSD3. The red oval points out the breaking of the jet on the free surface of the incoming flow.

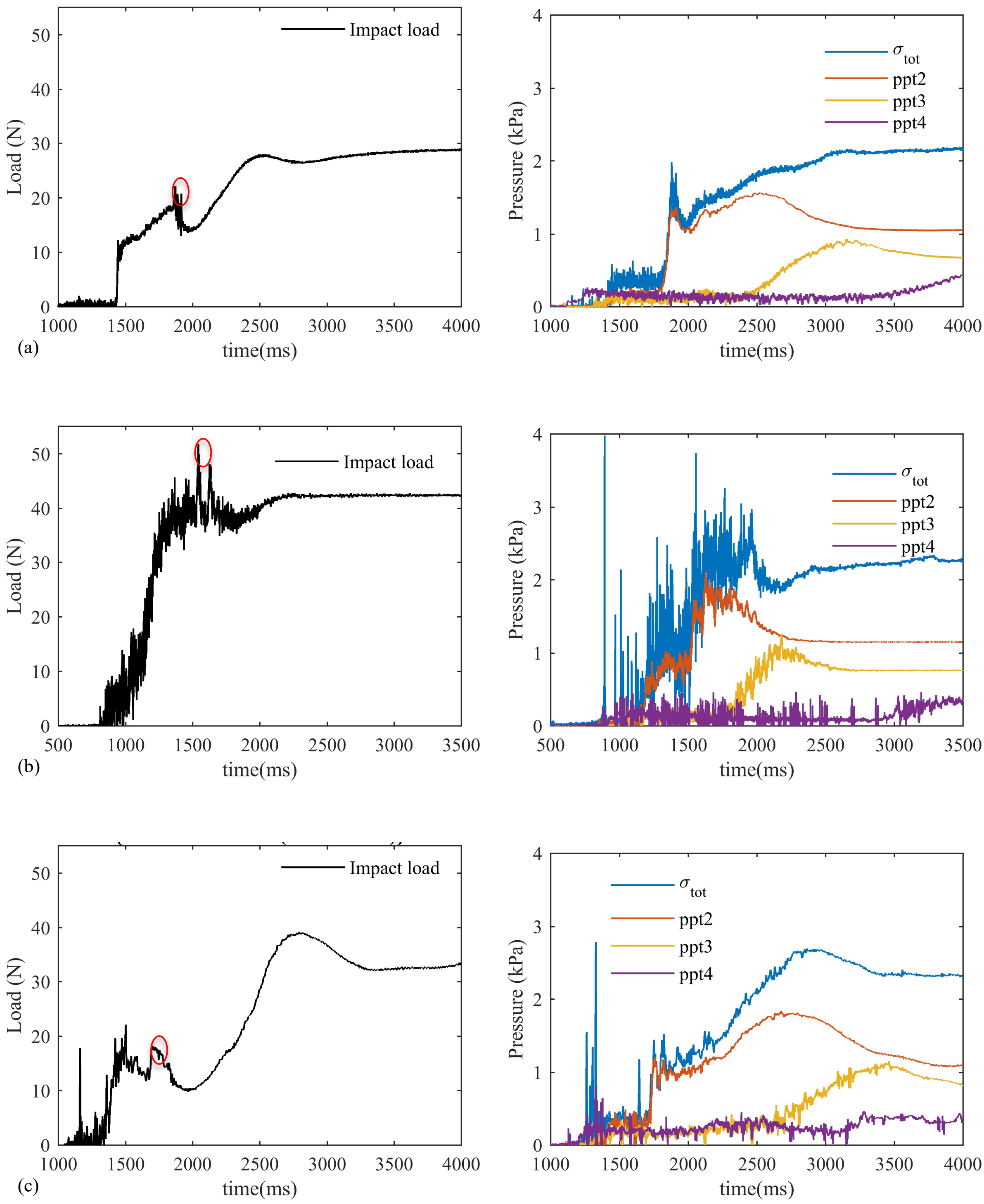

Figure 7. Fluid content 32% (Left) Load on barrier (Right) Basal pressures (a) PSD1, (b) PSD2, (c) PSD3. The red oval points out the breaking of the jet on the free surface of the incoming flow.